Spatial variability of liquid water path in marine low cloud: Part II. Climatology and dependence upon large-scale parameters.

ROBERT WOOD* and DENNIS. L. HARTMANN

University of Washington, Seattle, Washington

October 28, 2003

Abstract

In part I of this study we focused upon models to describe the mesoscale spatial variability of the cloud liquid water path. Here, we construct simple, exploratory, climatologies of the spatial variability characteristics of marine low clouds for two regions of the East Pacific. The climatologies show interesting and important geographical variability. Important differences between the mesoscale cloud structure over the NE and SE Pacific are observed. Large scale meteorological conditions are assessed for each MODIS scene using NCEP/NCAR reanalysis data, and regression analysis is used to assess relationships between large-scale forcings and mesoscale variability.

* *Corresponding author address:* Dr. Robert Wood, Atmospheric Sciences, University of Washington, Seattle, WA; *e-mail: robwood@atmos.washington.edu.*

1. Introduction

Spatial variability in marine boundary layer (MBL) low cloud is ubiquitous and is important both radiatively and dynamically (Cahalan et al. 1994; Rossow et al. 2002; Pincus and Klein 2000; Rotstayn 2000; Larson et al. 2001; Wood et al. 2002). Despite this importance, so far only limited attempts have been made to systematically quantify this variability over large regions of the oceans on timescales appropriate to large-scale numerical modeling. The situation is now improving with the introduction of an ISCCP mesoscale variability product (Rossow et al. 2002), which will provide a useful dataset for the investigation of the relationships between the large-scale and mesoscale spatial variability in low cloud.

In Part I of this study we presented a method for the breakdown of Moderate Resolution Imaging Spectroradiometer (MODIS) liquid water path data into 256×256 km "scenes" to which we then apply a number of analysis tools including probability density function (pdf) and power spectral analysis. We found that three variables (mean cloud-only liquid water path $\overline{LWP}$, cloud fraction CF, and the square of the ratio of the mean to standard deviation of cloud-only liquid water path γ_{LWP} provide a fairly complete description of the one point LWP statistics in MBL clouds. We also found that a simple Gaussian model of the saturation excess pdf (or, equivalently cloud thickness pdf) is quite successful at modeling the relationship between cloud fraction and cloud liquid water path variability. This model ties together the thermodynamic ahd cloud structure of the MBL in a way that may be suitable for parameterization in large-scale numerical models (see e.g. Park et al. 2003, which adopts an identical pdf form).

In Part II of this study, we continue our investigation into spatial variability characteristics in marine low cloud using MODIS. We focus here upon simple climatologies of the spatial variability characteristics for two regions of the East Pacific Ocean (see Part I for details of the regions studied). In addition, we extend our analysis using data from the NCEP/NCAR reanalysis, which allows an investigation into the relationships between mesoscale spatial variability and associated large-scale forcings. We also examine a scaling between mesoscale spatial variability and the MBL depth which may prove to be useful in the parameterization of mesoscale spatial variability and cloud fraction in MBL clouds.

2. Datasets used

a. MODIS

The dataset used in this study is presented detail in Part I, and only a brief description is given here. We use 1 km (at nadir) pixel data from the Moderate Resolution Imaging Spectroradiometer (MODIS) on the NASA Terra polar-orbiting sun-synchronous satellite. We use the MODIS Level 2 cloud product's visible/near-infrared algorithm (King et al. 1997) to estimate cloud optical thickness τ and near-cloud top effective radius $r_{e,top}$ resolution for daytime ($\sim$ 10:30 LST) scenes. We estimate liquid water path LWP from the $r_{e,top}$ and τ pixel data, and this LWP dataset is the primary dataset analysed. Only scenes containing exclusively warm cloud are analysed. Climatologies using two months of MODIS data (September/October 2000) are constructed on $2.5{\times}2.5^{\circ}$ grids that span the two study regions.

Boundary layer depth z_i is estimated using the method presented in Wood and Bretherton (2003), a novel technique that uses cloud top and sea surface temperature, cloud liquid water path, and the simple model of Park et al. (2003) to describe the temperature profile in deeper, decoupled boundary layers. Estimates of the accuracy of this technique are difficult to determine, but based upon the uncertainty in observations of cloud top and surface temperature, the uncertainty in derived z_i is probably smaller than 200 m.

The LWP pdf and the power spectrum are used to classify scenes as containing mesoscale cellular convection (MCC) of the open or closed form. A third classification includes homogeneous cloud in which MCC is either very weak or nonexistent. Open MCC has more skewed pdfs and more power at small scales than the closed form. P_{small} is defined here as the integrated power for $0.2 < k < 0.5$ km^{-1}, i.e.

$$P_{small} = \int_{0.2\ \mathrm{km}^{-1}}^{0.5\ \mathrm{km}^{-1}} P_{LWP} dk \tag{1}$$

Closed and open MCC cannot be diagnosed based upon cloud fraction alone because closed cellular convection covering only a small portion of the scene would be misdiagnosed as open celled convection. Fig. 1 shows an example of the diagnosis of open and closed cells. We diagnose *open* cellular convection as having (a) skewness larger than 1.8; (b) $P_{small} > 250$ g^2 m^{-4}; (c) cloud fraction $0.1 < CF < 0.75$. Of the remaining scenes, those with $\lambda_1 > 10$ km and $CF > 0.1$ are classified as *closed* mesoscale cellular convection. Those with $\lambda_1 \leq 10$ km and $CF > 0.1$ are classified as *homogeneous* cloud. Finally, those with $CF < 0.1$ are unclassified. These could either be scattered trade wind cumulus or edges of extensive stratocumulus.

Figure 1 shows the analysis applied to a larger (1168×1024 km) region where both open and closed MCC is present. We overlap the standard scenes to oversample because the Welch windowing technique removes data from the edges of scenes. The panel in the lower right shows the geographic distribution of the cell-type diagnosis corresponding to the main image which is in good agreement with those using visual analysis.

b. NCEP/NCAR reanalysis

We use NCEP/NCAR reanalysis data (Kistler et al. 2001) to investigate the links between large-scale meteorological parameters and mesoscale spatial variability. Our methodology is to obtain a set of pertinent reanalysis variables for each of the MODIS scenes analysed. The reanalysis data are available four times daily on a 2.5×2.5° grid, and include optimially-interpolated sea surface temperature data (Reynolds and Smith 1994). Trilinear interpolation is used to determine the values of the reanalysis variables at the scene-center location and time corresponding to each MODIS scene. We consider three NCEP-derived large-scale parameters in this study: lower tropospheric stability ($\theta_{700hPa} - \theta_0$, where θ is potential temperature); large-scale vertical motion at 850 hPa ($\overline{w_{850}}$); temperature advection $\mathbf{U} \cdot \nabla SST$, for which the NCEP surface wind and Reynolds SST gradient vectors are used. Because it is known that there exists a strong diurnal cycle in surface divergence and subsidence rates above the MBL (Dai and Deser 1999), we calculate the mean value for the 24 hour period centered on the time of the MODIS overpass for the 850 hPa vertical motion. This is not necessary for the other reanalysis parameters as their diurnal cycles are much weaker.

3. Climatology of mesoscale variability

Two months of MODIS data are used to create simple climatologies showing the geographical variations in the cloud mesoscale variability parameters. Data are binned into 2.5×2.5° regions to produce maps. The resolution for the mapping is chosen to ensure that the mapped fields show statistically significant geographical variability. The number of MODIS scenes contributing to each 2.5×2.5° average for the two month period is between 10 and 60.

a. LWP pdf parameters

Median values of $\overline{LWP}$ (cloud-only mean LWP) range from around 40 g m^{-2} to 80 g m^{-2} (Fig. 2(a,b)). In the NE Pacific, $\overline{LWP}$ increases slightly, from around 40-50 g m^{-2} in the stratus regions near the Californian coast, to around 60 g m^{-2} in the trade wind cumulus regions. The trend is quite similar in the SE Pacific, with low values close to the Chilean coast, increasing downwind. However, $\overline{LWP}$ tends to decrease again in the SE Pacific trade winds. A general feature (not shown) is that in regions with high climatological cloud fraction ($\overline{CF} > 0.6$), $\overline{LWP}$ is positively correlated with CF, whereas there is little correlation for regions where the mean CF is lower.

An alternative way at examining the LWP pdf uses the Gaussian model (see Part I) to obtain a 1:1 mapping of $[\overline{LWP}, CF]$ into mean and standard deviation of cloud layer thickness $[\overline{h}, \sigma_h]$, or alternatively $[\overline{s_i}, \sigma_{s_i}]$, where h is cloud thickness and s_i the saturation excess at the MBL inversion base. We assume here that the cloud is adiabatic with a constant Γ_{ad}=2 g kg^{-1} km^{-1}. Figure 3 shows this 1:1 mapping with SE Pacific MODIS data. Although the Gaussian model is not a perfect description of one point LWP statistics (see Wood and Hartmann 2004, part I of this study, for evaluation), these models relate the LWP variability to variability in the geometrical and thermodynamic structure of the cloud layer.

Using this mapping, a number of interesting and important points emerge. First, the MODIS data are clustered around lines of constant $\overline{LWP}$, so that only rarely do scenes have mean LWP larger than 150 g m^{-2} or less than 25 g m^{-2}. Perhaps surprisingly, these limits seem to be relatively independent of CF suggesting that there may be universal physical upper and lower limits upon cloud liquid water path in marine boundary layer clouds. We hypothesize that the upper limit is imposed by a drizzle negative feedback. Increased LWP results in more drizzle which stabilizes the MBL and suppresses moisture transport from the surface. The lower limit may be associated with longwave radiative feedback that leads to instability in very thin cloud layers, which causes either rapid thickening or dissipation (Paluch and Lenschow 1991). Indeed, radiative transfer calculations suggest that the longwave cooling efficiency starts to weaken in clouds with LWP less than 25-50 g m^{-2}. Second, σ_h (or σ_s) is inversely correlated with $\overline{h}$ (or $\overline{s_i}$) as the clouds transition from overcast stratocumulus to broken trade-wind cumulus. This increasing mesoscale variability in the Sc-Cu transition is strongly related to the properties of the MCC and boundary layer depth (see Section **3.5.**), with the source of variability in h (or s) related to the increasing decoupling of the cloud layer from the surface mixed layer.

Maps of CF and γ_{LWP} (Fig. 2(c-f)) demonstrate the strong connection between these parameters examined in part I of this study. The most homogeneous LWP (and the highest CF) is found along the Californian and Chilean coasts, and decreases towards the remote ocean and trade-wind regions. The coverage of both unbroken (e.g. $CF > 0.6$) and homogeneous cloud (e.g. $\gamma_{LWP} > 2$) is more extensive in the SE than in the NE Pacific during this season. A longer dataset is required to determine whether the $CF - \gamma_{LWP}$ links exist on seasonal timescales, and therefore be useful for parameterizing unresolved variability in climate models. In the SE Pacific, the clouds remain unbroken and quite homogeneous right into the tropical equatorial region, quite unlike the situation in the NE Pacific. This reflects differences in the SST patterns and prevailing winds in the two regions which give rise to stronger cold advection in the stratocumulus to cumulus transition regions of the NE Pacific. This stronger cold advection most likely hastens the decoupling process and rate of BL deepening by increasing surface fluxes. Figure 4 shows mean z_i for September/October 2000. Boundary layers originating close to the Chilean coast deepen far less rapidly (in the Lagrangian sense) than those along the Californian coast as they advect equatorwards. Therefore, the effect of boundary layer deepening upon decoupling Bretherton and Wyant (1997) is probably less in the SE Pacific. Mean NCEP estimated subsidence rates at the BL top in both regions are comparable, and so the more static boundary layer depths (in a Lagrangian sense) in the SE Pacific may be attributed to lower entrainment rates (Wood and Bretherton 2003), possibly due to stronger inversions.

b. Characteristic lengthscale

Figure 5 shows the median charactertistic cell lengthscale λ_1. We only consider scenes with $CF > 0.2$ because obtaining λ_1 from relatively cloud free scenes is more uncertain. The smallest cells (< 20 km) are found over the cold water close to the Oregon/Californian coast, with a strong oceanward gradient. Median values of λ_1 reach a maximum of around 40-45 km as the subtropical airmass advects over warmer waters and the boundary layer deepens. SE Pacific values show a somewhat similar trend with the smallest values associated with regions of climatologically shallow boundary layers (see Fig. 4). As in the NE Pacific, median values reach around 40-45 km in the trades. An important link between cell size, subgridscale variance and boundary layer depth is explored in Section **3. 5.**.

c. Homogeneous Open or closed mesoscale cellular convection?

Figure 6 shows a climatology of the prevalence of homogeneous cloud (no MCC), closed MCC, and open MCC, estimated for each MODIS scene using the method described in section 2a. The fraction of homogeneous clouds is small apart from north of 40N, along the Californian/Baha coastline, and close to the Chilean coasts, all regions with the shallowest mean z_i (Fig. 4), and regions containing the highest fraction of boundary layers shallower than 800 m. Closed MCC dominates throughout much of the NE and SE Pacific, occurring in over 60% of the scenes over the coldest waters of the NE and SE Pacific. Closed MCC is very common along the entire equatorial region out to 120W, ocurring $> 80\%$ of the time between 5S and the equator. Open MCC dominates over the warmer water trade-wind regions of the SE and NE Pacific, and to the north of the equatorial cold tongue. The diagnosis of open MCC also includes heterogeneous mesoscale rolls that seem to be peculiar to the region north of the equatorial cold tongue. It should be noted that it is perhaps inappropriate to classify these rolls as open MCC, but further subclassification of the groups was not attempted in this study.

The transition (in a Lagrangian sense of a moving air parcel) from homogeneous-dominated, through closed and then open MCC regions can be conceptualized as the stratocumulus to cumulus transition (SCT, Bretherton and Pincus 1995; Bretherton et al. 1999; de Roode and Duynkerke 1997), with the most homogeneous clouds being stratus, the closed MCC being stratocumulus, and the open MCC being dominated by cumuliform cloud. By examination of typical boundary layer trajectories in the two regions (not shown), it is clear that whilst there is a clear SCT transition in the NE Pacific, the persistence of closed MCC along trajectories in the SE Pacific does not consititute an SCT in the typical manner that it is observed in the NE Atlantic and Pacific. This could be a consequence of the more constant MBL depth along SE Pacific trajectories, preventing the warming-deepening decoupling process Bretherton and Wyant (1997) from becoming an important factor in the evolution of cloud in the SE Pacific.

4. The influence of large-scale parameters

Klein (1997) demonstrates that both lower tropospheric stability and temperature advection (cold advection positive) are positively correlated with nighttime low cloud amount at ocean weather station November (30N, 140W) in the subtropics. Our data also support these general findings, although in this study we focus additionally upon the large-scale influence upon parameters related to the spatial variability in low cloud fields - $\overline{LWP}$, γ_{LWP} and the characteristic length scale λ.

a. Regression maps of daily data

Maps showing the regression of cloud-mean liquid water path $\overline{LWP}$, cloud fraction CF, and homogeneity parameter γ_{LWP} onto large scale parameters are shown in Figs. 7 ($\overline{w_{850}}$), 8 (lower tropospheric stability), and 9 (temperature advection). Regressions were performed by first averaging the data from all the MODIS scenes in a 5×5° resolution grid for each day to create a daily timeseries at each gridbox. Not all days at each location contain data but this is not important for regression analysis.

The cloud-mean LWP is influenced strongly by $\overline{w_{850}}$ in the NE Pacific stratocumulus region, especially close to the Californian coast, with positive anomalies in 850 hPa vertical wind (reduced subsidence) associated with increased $\overline{LWP}$. Little effect is observed elsewhere, except in the trade-wind and tropical regions of the SE Pacific, where a similar correlation is found. Vertical wind is uncorrelated with cloud fraction everywhere, and only weakly correlated with γ_{LWP} off the Baha peninsular, where increased subsidence favors more homogeneous cloud.

Lower tropospheric stability is found to be uncorrelated with $\overline{LWP}$ in the NE Pacific, and only for a small region of the SE Pacific. However, increased stability is strongly correlated with cloud fraction in both the NE and SE Pacific subtropical regions, particularly those marked by high climatological cloud fraction. This correlation, which has been explored in previous work (e.g. Slingo 1980, 1987; Klein and Hartmann 1993; Klein 1997) forms the basis for the parameterization of low cloud in a number of large-scale numerical models. Klein and Hartmann (1993) show that the relationship between stability and cloud amount is remarkably strong on seasonal timescales and over large regions. The evidence in Fig. 8 suggests that this relationship exists on scales of days to weeks, and on quite small geographical scales. However, this correlation becomes much weaker in the trade-wind regions, but this may be in part because the degree of day-to-day variability in both cloud amount and tropospheric stability in the trade wind regions is much weaker. A longer time record of daily data is required to establish whether the cloud amount-stability correlations truly disappear on daily to weekly timescales in the trade-wind regions.

Another surprise is that in the SE Pacific, the correlation becomes small in the region east of 100W and north of 15S (coastal Peruvian region), which is a region dominated by stratocumulus clouds. Indeed, cloud fraction is found to be uncorrelated with any of the large scale parameters (or boundary layer depth) in this region. Why this should be is unclear, but it might be useful to speculate on possible causes. First, in this region both the cloud fraction variability and lower tropospheric stability are markedly smaller than anywhere to the south and west, and anywhere in the NE Pacific stratocumulus region (Fig. 10). This is likely related to the moderating influence of the Andes mountains on the tropospheric temperatures over the far Eastern Pacific. Thus, even if stability and cloud fraction are related in this region, it is easier for additional physical factors (or noise) to drown out signals in the regressions. Free-tropospheric moisture does not correlate with cloud fraction in this region (no significant correlations with cloud fraction are found anywhere in the NE or SE Pacific, except to the north of the equatorial cold tongue). Second, the lack of clear controlling factors for cloud amount could hint at an internal source for cloud fraction variability in the coastal Peruvian region, which might involve aerosol-drizzle-cloud feedbacks. This is difficult to investigate with the current dataset, because effective radius retrievals are known to be biased in regions of broken, inhomogeneous cloud (Graeme Stephens, personal communication), and thus spurious correlations between these two variables are likely to arise.

In order to be consistent with the Gaussian-s model, increased stability must increase γ_{LWP} as well as CF and increased $\overline{w_{850}}$ should not be correlated with γ_{LWP}. This is indeed the case in the regions with marked stability-CF correlations.

Temperature advection (Fig. 9) is only weakly correlated with $\overline{LWP}$, but is quite well correlated with cloud fraction, particularly in the stratocumulus to cumulus transition region of the NE Pacific (as found in Klein 1997), in the stratocumulus regions south of 20S, and to the north of the equatorial cold tongue, where particularly strong cold advection results in strong surface forcing (deSzoeke and Bretherton 2004), and tropical instability waves provide important modulation of the surface fluxes (Thum et al. 2002).

Fig. 11 demonstrates that z_i has very little correlation with $\overline{LWP}$, and only weak correlation with cloud fraction. This is surprising because the patterns of geographical variability in mean cloud fraction (Fig. 2) and boundary layer depth (Fig. 4) are remarkably similar. Stability and z_i are strongly negatively correlated (r=-0.4 to -0.7) in the regions where stability and cloud fraction are strongly positively correlated (Fig. 12), which makes the lack of $z_i - CF$ correlation in these areas somewhat intriguing. Although boundary layer depth is clearly influenced by stability on daily-weekly timescales, it does not appear to be the z_i fluctuations themselves that are modulating the cloud fraction.

In the NE Pacific there is a large region where MBL depth and γ_{LWP} are negatively correlated.

In the SE Pacific, this correlation is small apart from at the south of the region. The MBL depth appears to have a generally larger influence upon cloud homogeneity on the short timescale than it does upon the cloud amount, particularly in the NE Pacific. This may be because MBL and cloud inhomogeneity is closely tied to the characteristic lengthscale of mesoscale cells, which are well correlated with z_i, particularly in the regions of extensive stratocumulus clouds (not shown). We return to this scaling of mesoscale features with MBL depth in Section 5.

To assess the key driving force for the modulation of clouds and large scale forcings on daily to monthly timescales, we use autocorrelation analysis on the daily timeseries for each $5\times5^{\circ}$ gridbox. Regular Fourier spectral analysis is precluded because each gridbox does not contain data on every day during the analysis period. Autocorrelation data are obtained for each series at lags of 1-30 days, and for each series with at least 50% of the maximum possible data points we estimate the non-zero lag at which the series becomes best correlated again with itself. This lag is the dominant timescale and coincides with the period of the dominant mode of variability. This timescale is plotted in Fig. 13 as a function of latitude. Several key points are noted. First, the dominant timescales are mostly in the range 7-12 days and do not vary strongly with latitude. Spectral analysis of midlatitude geopotential fields reveals a dominant mode of variability with an approximate 10 day period (Fraedrich and Bottger 1978) corresponding to eastward propagating long waves. Hakim (2003) demonstrate that these waves are, in fact, midlatitude wave packets forming in the North Pacific storm track, and that they frequently penetrate deep into the subtropics, and sometimes the tropics. Second, the timescales of cloud and forcing parameters are approximately equal confirming that the variability in subtropical clouds on daily to weekly timescales is governed largely by variability in large-scale forcings. The lack of strong latitudinal trends in the dominant timescale of the forcing parameters suggests that the effects of baroclinic instability is probably the most important driver of the variability of subtropical clouds on daily to monthly timescales.

b. Geographical variation of means

Geographical variations of the mean large-scale parameters corresponding to the MODIS scenes are shown in Fig. 14. Subsidence dominates the boundary layer cloud cases throughout most of the NE and SE Pacific regions, but boundary layer clouds are also found in regions of large-scale ascent, most notably in the ITCZ regions at latitudes of 5-15N. There also appears to be strongly reduced subsidence, and even ascent, close to the northern Chilean coast, which may be related to a mountain-influenced sea-breeze structure (Garreaud and Muñoz 2004), although it cannot be ruled out as an artifact of the reanalysis data upstream of strongly sloping terrain. Strong lower tropospheric stability also dominates the eastern Pacific regions, particularly over the coastal upwelling regions of the subtropics. Temperature advection is largely positive (i.e. cold advection) throughout the two regions, apart from very close to the northwestern United States coastline and along the equatorial cold tongue. Very strong cold advection is observed to the north of the cold tongue as cool air flows northwards over a strong gradient in sea surface temperature.

Geographical variations of climatological mean cloud fraction as a function of both stability and boundary layer depth are examined on the longer two monthly timescale using the $2.5\times2.5^{\circ}$ means (Figure 15). We only include SE Pacific data south of the equator; data from north of the equatorial cold tongue will be discussed below. In addition, we should emphasize that the mean cloud amounts discussed here are the mean values for the daytime (10:30 am local time) MODIS overpasses. Given that diurnal maxima in cloud fraction and mean liquid water path occurs typically at 3-6 am (Rozendaal et al. 1995; Wood et al. 2002), the MODIS cloud amounts (measured ∼6 hours after the peak) are fairly representative of the diurnal mean cloud amount.

There is a tight correlation between mean stability and CF (r=0.86 and 0.90 for the NE and SE Pacific subtropical regions) which holds through the entire range of mean cloud amounts observed (∼0.2 to ∼0.9). The best fit is close to that found for the climatological mean cloud amounts for a number of regions (Klein and Hartmann 1993), although we find the sensitivity of the mean cloud amount to the stability to be 20% greater (0.075 increase in cloud fraction per degree of stability increase). The correlations between mean CF and z_i are almost as high as for stability (0.81 and 0.87 for the NE and SE Pacific respectively), which is surprizing given the lack of regression on short timescales between these parameters. Data from regions where little correlation exists on the short timescales (such as the coastal Peruvian region discussed above) fall onto the well-correlated spread in data, suggesting that low variability *in these regions* may be primarily responsible for the poor daily correlations. However, in regions where stability is well correlated with CF and z_i, reduced variability is not responsible for the poor z_i, CF correlations.

c. *What controls cloud fraction and homogeneity?*

Reduced variability in some regions does not explain why the climatological coupling between z_i and CF is so tight and yet the daily correlations are so small. Hypotheses for why increasing stability tends to increase the cloud amount include: (i) greater lower tropospheric stability requires more work be done against stratification in order to deepen a boundary layer, so that, for a given entrainment rate, higher stability will lead to shallower boundary layers. Shallower boundary layers are more likely to remain well-mixed (Bretherton and Wyant 1997) so that the cloud layer remains connected to the oceanic moisture supply. Deeper boundary layers on the other hand are more likely to decouple, and this decoupling results in cloud breakup; (ii) entrainment is limited by strong stability, and this prevents the incorporation of warm, dry air into the boundary layer. A cooler, moister boundary layer will be more favourable for the maintenance of cloud. On the seasonal mean timescale it appears that hypothesis (i) is supported by the data, with the largest mean cloud fractions being associated with the greatest stability and shallowest boundary layers. However, on the daily timescale (i) is not supported by the data, leading to speculation that although increased stability is associated with shallow z_i, it is the stability itself, rather than the boundary layer depth *per se* that controls the cloud cover.

This leaves the possibility that hypothesis (ii) is the most important effect of increased stability. There is some support for hypothesis (ii) Wood and Bretherton (2003) show that the mean entrainment rate is roughly constant throughout the subtropical NE and SE Pacific, even as the cloud fraction decreases markedly downwind in the trades. Thus, for a given inversion strength, cloudy boundary layers tend to entrain far more efficiently than clear ones due to the effects of latent heat release in cloud and longwave cooling at cloud top (e.g. Nicholls and Turton 1986). Therefore, the lack of a clear relationship between mean entrainment rate and cloud fraction in the subtropics (Wood and Bretherton 2003) suggests that greater stability in cloudy regions is limiting the entrainment rate there, consistent with hypothesis (ii). However, there is no available data at present to examine this relationship on the daily timescale. We hope that an extensive Lagrangian-type analysis of high temporal resolution GOES data may be able to address this hypothesis on short timescales.

A possible problem with hypothesis (ii) is that within a mixed layer framework, forced with boundary conditions and advective tendencies appropriate for the subtropical high pressure regions, cloud thickness is actually an *increasing* function of the entrainment rate and boundary layer depth. This is because although entrainment raises the LCL (cloud base height) by warming and drying the MBL, it also raises the inversion (i.e. cloud top) height. The rise (in the Lagrangian sense) in cloud top height tends to be larger than the rise in LCL, leading to a thickening cloud layer. Therefore, if the MBL over the subtropical eastern oceans could be suitably described by a mixed layer, then reduced entrainment rates would result in thinner clouds. The resolution is either that hypothesis (ii) is incorrect, or that the mixed layer framework is inadequate to describe much of the subtropical MBL.

5. Scaling of mesoscale variability

Figure 16 shows the median characteristic cell lengthscale λ_1 binned as a function of boundary layer depth z_i. When the boundary layer depth is greater than 600-800 m, the cells tend to organize with preferred aspect ratios (horizontal:vertical cell scale) in the range 30-40. There is considerable variation of this aspect ratio from scene to scene, as might be expected if some considerable time is required for cells to equilibrate at their preferred scale (see e.g. Shao and Randall 1996). For example, for boundary layers between 1200-1300 m deep, the 25th, 50th and 75th percentiles of λ_1 are 31, 41 and 63 km respectively, indicating a considerable range within each z_i class. However, it is unclear as to whether this spread is caused by random errors and ambiguity in the determination of λ_1 from the MODIS scenes, or whether it represents true departure from the constant aspect ratio hypothesis. Departures could be caused by cell the equilibration timescale being comparable or longer than the boundary layer growth timescale. Lagrangian studies of evolving MCC using geostationary satellites may prove to be a useful tool to resolve these issues.

For boundary layers shallower than 600-800 m there is a marked decrease in the cell aspect ratio. This suggests that the growth of MCC cannot be supported in well-mixed shallow boundary layers. Indeed, for $z_i < 600$ m mesoscale cells are seldom observed in our dataset. This result provides some support for the conceptual model proposed by Shao and Randall (1996) whereby the production of mesoscale cellular convection requires the presence of a stable layer in the middle of the cloud-topped boundary layer. Such stable layers are associated with the decoupling of the marine boundary layer, a phenomenon rarely observed in boundary layers shallower than 600 m or so. It is perhaps possible that the presence or absence of mesoscale cells might be a sensitive indicator of boundary layer decoupling. To be tested, this speculation would require additional investigation with a combination of satellite and in-situ data.

An automatic classification procedure described above allows us to determine whether the mesoscale convective cells in each scene are of open or closed type. With this classification we show that the $\lambda_1 - z_i$ relationships for open and for closed cells are almost the same when the boundary layer is deeper than 800 m (not shown). However, closed cells are much the commoner type of MCC when the boundary layer is shallower (constituting 83% of the MCC scenes when $800 < z_i < 1200$, but only 38% in boundary layers deeper than 2000 m). From this we hypothesize that the cell scale is not determined by whether the cells are open or closed, but that open MCC becomes more favourable in deeper boundary layers. Although the Shao and Randall conceptual model for closed MCC may indeed be driven by cloud top radiative cooling, it is difficult to account for open MCC with this mechanism. This leads one to wonder if it is purely coincidental that there appears to be no systematic difference between the median aspect ratios in open and closed MCC. Or, is a single mechanism responsible for the generation of the two types of MCC?

The cell scale is an important parameter because it is closely tied to the degree of subgridscale variance in saturation excess. In Part I a method was presented to estimate the standard deviation of the saturation excess σ_s in the cloud layer, using MODIS observations of the LWP pdf. In Figure

17 we show plots of median σ_{LWP} and median estimated σ_s against cell scale λ_1 and boundary layer depth z_i. Both σ_{LWP} and σ_s increase as λ_1 increases, indicating that enhanced mesoscale variance in relative humidity and consequently LWP is associated with larger cells. Near-linear relationships are found between $\sigma_{LWP} - z_i$ and $\sigma_s - z_i$. Also shown are median values from a number of intensive field programs (Wood and Taylor 2001; Wood et al. 2002; Bretherton et al. 2003) in subtropical marine boundary layers in the NE Atlantic (ASTEX), NE Pacific (FIRE) and SE Pacific (EPIC). Aircraft observations and microwave radiometer LWP are derived from reliable measurements and provide support that a general scaling exists between mesoscale variability and boundary layer depth, and is intimately coupled through the mechanism of MCC cell growth.

6. Discussion and conclusions

In Part II of this study we have presented an initial attempt at producing a climatology of low cloud mesoscale variability over the NE and SE Pacific Ocean, using 1 km resolution data from MODIS. We have used a number of parameters, discussed in more depth in Part I of the study, that best characterize the mesoscale spatial variability in MBL cloud. We find that three parameters (cloud fraction, mean in-cloud liquid water path, and the square of the ratio of the mean to standard deviation of the cloud-only liquid water path) provide a reasonably complete description of the one point statistics of cloud liquid water path mesoscale spatial variability. We also found that cloud homogeneity is strongly coupled with the cloud fraction, and that the spatial variability in cloud can be coupled quite effectively to variability in the underlying thermodynamic parameters using a simple Gaussian model of saturation excess.

In Part II, we have examined how these parameters vary in relation to large-scale forcings from NCEP reanalysis products, using both regressions of daily gridded data and by examining the geographical variability of mean values. The results suggests that both cloud cover and the mesoscale spatial variability within cloud are modulated by fluctuations in forcing variables, particularly the lower tropospheric stability (Klein and Hartmann 1993) and temperature advection (Klein 1997). In many places, most notably off the coast of Peru, cloud cover and spatial variability does not correlate strongly with any of the forcing variables examined, but this may be because the daily to monthly variability is very low.

While there are very good relationships between $2.5\times2.5^{\circ}$ means of cloud fraction and both stability and boundary layer depth, the regression analysis shows that CF variations are not strongly correlated with z_i. This suggests that it may be variation in entrainment rate, rather than z_i *per se* that controls the cloud fraction.

Cloud homogeneity γ_{LWP} correlates with z_i in regions where the $CF-z_i$ correlations are poor, suggesting that the mesoscale variability may indeed be more strongly controlled by boundary layer depth than entrainment rate. The observed couplings between mesoscale LWP/saturation excess variance, the characteristic lengthscale of the mesoscale cellular convection (MCC), and the boundary layer depth, are good evidence that there may exist universal scalings between the boundary layer depth and the thermodynamic/cloud spatial variability properties in the MBL. These may be useful, both in offering insight into the processes controlling mesoscale spatial variability in MBL clouds, and for future development of parameterizations to account for such variability.

References

Bretherton, C. S., S. K. Krueger, M. C. Wyant, P. Bechtold, E. vanMeijgaard, B. Stevens, and J. Teixeira: 1999, A gcss boundary layer model intercomparison study of the first astex lagrangian experiment. *Bound. Layer Meteorol.*, **93**, 341–380.

Bretherton, C. S. and R. Pincus: 1995, Cloudiness and marine boundary layer dynamics in the astex lagrangian experiments. part i: Synoptic setting and vertical structure. *J. Atmos. Sci.*, **52**, 2707–2723.

Bretherton, C. S., T. Uttal, . Fairall, C. W., . Yuter, S. E., . Weller, R. A., . Baumgardner, D., . Comstock, K., and R. Wood: 2003, The epic 2001 stratocumulus study. *Bull. Am. Meteorol. Soc.*, in review.

Bretherton, C. S. and M. C. Wyant: 1997, Moisture transport, lower-tropospheric stability, and decoupling of cloud-topped boundary layers. *J. Atmos. Sci.*, **54**, 148–167.

Cahalan, R. F., W. Ridgway, W. J. Wiscombe, T. L. Bell, and J. B. Snider: 1994, The albedo of fractal stratocumulus clouds. *J. Atmos. Sci.*, **51**, 2434–2455.

Dai, A. and C. Deser: 1999, Diurnal and semidiurnal variations in global surface wind and divergence fields. *J. Geophys. Res.*, **104**, 31109–31125.

de Roode, S. R. and P. G. Duynkerke: 1997, Observed lagrangian transition of stratocumulus into cumulus during astex: mean state and turbulence structure. *J. Atmos. Sci.*, **54**, 2157–2173.

deSzoeke, S. P. and C. S. Bretherton: 2004, Quasi-lagrangian large eddy simulations of cross-equatorial flow in the east pacific atmospheric boundary layer. *J. Atmos. Sci.*, submitted.

Fraedrich, K. and H. Bottger: 1978, A wavenumber-frequency analysis of the 500 mb geopotential at 50°n. *J. Atmos. Sci.*, **35**, 745–750.

Garreaud, R. D. and R. Muñoz: 2004, The diurnal cycle in circulation and cloudiness over the subtropical southeast pacific: A modeling study. *J. Clim.*, in press.

Hakim, G. J.: 2003, Developing wave packets in the north pacific storm track. *Mon. Wea. Rev.*, **131**, 342–355.

King, M. D., S.-C. Tsay, S. E. Platnick, M. Wang, and K.-N. Liou: 1997, Cloud retrieval algorithms for modis: Optical thickness, effective particle radius, and thermodynamic phase. MODIS Algorithm Theoretical Basis Document ATBD-MOD-05, NASA.

Kistler, R., E. Kalnay, W. Collins, S. Sana, G. White, J. Woolen, M. Chelliah, W. Ebisuzaki, M. Kanamitsu, V. Kousky, H. van den Dool, R. Jenne, and M. Fiorino: 2001, The ncep/ncar 50-year reanalysis. *Bull. Am. Meteorol. Soc.*, **82**, 247–267.

Klein, S. A.: 1997, Synoptic variability of low-cloud properties and meteorological parameters in the subtropical trade wind boundary layer. *J. Climate*, **10**, 2018–2039.

Klein, S. A. and D. L. Hartmann: 1993, The seasonal cycle of low stratiform clouds. *J. Climate*, **6**, 1588–1606.

Larson, V. E., R. Wood, P. R. Field, J.-C. Golaz, T. H. Vonder Haar, and W. R. Cotton: 2001, Systematic biases in the microphysics and thermodynamics of numerical models that ignore subgrid-scale variability. *J. Atmos. Sci.*, **58**, 1117–1128.

Nicholls, S. and J. D. Turton: 1986, An observational study of the structure of stratiform cloud sheets: Part ii. entrainment. *Quart. J. Roy. Meteorol. Soc.*, **112**, 461–480.

Paluch, I. R. and D. H. Lenschow: 1991, Stratiform cloud formation in the marine boundary layer. *J. Atmos. Sci.*, **48**, 2141–2158.

Park, S., C. B. Leovy, and M. A. Rozendaal: 2003, A new single column marine boundary layer cloud model. *J. Atmos. Sci.*, submitted.

Pincus, R. and S. A. Klein: 2000, Unresolved spatial variability and microphysical process rates in large scale models. *J. Geophys. Res.*, **105**, 27059–27066.

Reynolds, R. W. and T. M. Smith: 1994, Improved global sea surface temperature analyses using optimum interpolation. *J. Clim.*, **7**, 929–948.

Rossow, W. B., C. Delo, and B. Cairns: 2002, Implications of the observed mesoscale variations of clouds for earth's radiation budget. *J. Clim.*, **15**, 557–585.

Rotstayn, L. D.: 2000, On the ”tuning” of autoconversion parameterizations in climate models. *J. Geophys. Res.*, **105**, 15,495–15,507.

Rozendaal, M. A., C. B. Leovy, and S. A. Klein: 1995, An observational study of the diurnal cycle of marine stratiform cloud. *J. Clim.*, **8**, 1795–1809.

Shao, Q. and D. A. Randall: 1996, Closed mesoscale cellular convection driven by cloud-top radiative cooling. *J. Atmos. Sci.*, **53**, 2144–2165.

Slingo, J. M.: 1980, A cloud parameterization scheme derived from GATE data for use with a numerical model. *Quart. J. Roy. Meteorol. Soc.*, **106**, 774–770.

— 1987, The development and verification of a cloud prediction scheme for the ecmwf model. *Quart. J. Roy. Meteorol. Soc.*, **113**, 899–927.

Thum, N., S. K. Esbensen, D. B. Chelton, and M. J. McPhaden: 2002, Air-sea heat exchange along the northern sea surface temperature front in the eastern tropical pacific. *J. Clim.*, **23**, 3361–3378.

Wood, R. and C. S. Bretherton: 2003, Boundary layer depth, entrainment and decoupling in the cloud-capped subtropical and tropical marine boundary layer. *J. Clim.*, submitted.

Wood, R., P. R. Field, and W. R. Cotton: 2002, Autoconversion rate bias in boundary layer cloud parameterizations. *Atmos. Res.*, **65**, 109–128.

Wood, R. and J. P. Taylor: 2001, Liquid water path variability in unbroken marine stratocumulus. *Quart. J. Roy. Meteorol. Soc.*, **127**, 2635–2662.

Figure Captions

Figure 1: A 1168×1024 km portion of MODIS swath data showing regions of closed and open cellular convection and the method used to diagnose these regions from the 245×256 km scenes. Two example scenes (Op and Cl) chosen from the large image are chosen as representative of regions containing open (subregion on lower left of image) and closed (subregion to upper right) cellular convection. (a) power spectra kP_{LWP} are plotted as a function of total wavenumber k showing that the open celled convection contains more power at wavenumbers greater than 0.2 km^{-1} (5 km); (b) The LWP pdfs for the open celled region is more skewed than that for the closed celled region; (c) a plot of the integrated power P_{small} in the 0.2-0.5 km^{-1} range plotted against the LWP pdf skewness S_{LWP}. Open celled images are diagnosed by requiring $S_{LWP} > 1.8$ and $P_{small} > 250$ g^2 m^{-4} and cloud fraction CF (total fraction of points in the scene diagnosed as cloudy) in the range $0.1 < CF < 0.75$; (d) the location of those regions of the main image that have been diagnosed as open and closed. See text for further details. Note that image is rotated for display purposes so that the approximate direction west is towards the top of the page.

Figure 2: Climatological mean value of $\overline{LWP}$ (a,b), CF (c,d), and climatological median value of γ_{LWP} (e,f) for all September/October MODIS scenes in the NE and SE Pacific.

Figure 3: $\overline{LWP}$ (dotted lines) and CF (dashed lines) in the [$\overline{h}$,σ_h] plane for the Gaussian-h model 1:1 mapping. Upper and right axes show equivalent $\overline{s_i}$ and σ_s for Gaussian-s model with zero cloud top height fluctuations and Γ_{ad}=2 g kg^{-1} km^{-1}. Contours show joint pdf of values from

all SE Pacific MODIS data, and contain 95%, 80%, 50%, 30%, and 10% of all scenes.

Figure 4: Mean boundary layer depth for all warm cloud scenes in the NE (a) and SE (b) Pacific, Sept/Oct 2000.

Figure 5: Median values of the characteristic lengthscale for all scenes with $CF > 0.2$ for the NE (a) and SE (b) Pacific regions.

Figure 6: Fraction of MODIS scenes diagnosed as homogeneous cloud (a,b), closed MCC (c,d), and open MCC (e,f), for the NE and SE Pacific.

Figure 7: Correlation coefficient between w_{850} and $\overline{LWP}$ (a,b), CF (c,d), and γ_{LWP} (e,f), for NE (left) and SE (right) Pacific MODIS data. In this, and all subsequent regression maps, shaded areas indicate regions where the correlations are significant at the 95% level. Non-significant correlations are not contoured.

Figure 8: Correlation coefficient between lower tropospheric stability and $\overline{LWP}$ (a,b), CF (c,d), and γ_{LWP} (e,f), for NE (left) and SE (right) Pacific MODIS data.

Figure 9: Correlation coefficient between temperature advection and $\overline{LWP}$ (a,b), CF (c,d), and γ_{LWP} (e,f), for NE (left) and SE (right) Pacific MODIS data.

Figure 10: Cloud fraction (a,b) and lower tropospheric stability (c,d) standard deviation in the

NE and SE Pacific.

Figure 11: Correlation coefficient between boundary layer depth and $\overline{LWP}$ (a,b), CF (c,d), and γ_{LWP} (e,f), for NE (left) and SE (right) Pacific MODIS data.

Figure 12: Correlation coefficient between boundary layer depth and lower tropospheric stability for NE (a) and SE (b) Pacific data.

Figure 13: Dominant timescales for modulation of cloud structural parameters (a) and large scale forcings (b), plotted as a function of latitude for the NE and SE Pacific regions. Error bars show the 2-σ estimated uncertainty in the mean timescale, estimated using the available 5$\times$5° grid-box data at each latitude.

Figure 14: Mean values of 850 hPa vertical wind w_{850} (a,b), lower tropospheric stability $\theta_{700hPa} - \theta_0$ (c,d), and temperature advection $\mathbf{U} \cdot \nabla SST$ (e,f) for the corresponding MODIS scenes in the NE (left) and SE (right) Pacific during September/October 2000.

Figure 15: (a) Two-monthly mean values of MODIS scene cloud fraction as a function of lower tropospheric stability. Each point represents a single 2.5$\times$2.5° region. The dotted line shows the results of Klein and Hartmann (1993) and the dashed line the best fit to the MODIS data for the NE and SE Pacific. (b) Cloud fraction as a function of MODIS-derived boundary layer depth.

Figure 16: Median characteristic cell lengthscale λ_1 binned by boundary layer depth z_i for all

MODIS scenes (solid circles) over the NE and SE Pacific. The dotted lines denote aspect ratios of 20:1, 30:1 and 40:1. Error bars indicate the approximate sampling error in the median. The solid line indicates the fit described in the text.

Figure 17: Standard deviations of liquid water path σ_{LWP} (a,b) and saturation excess σ_s (c,d) plotted against cell scale λ_1 (a,c) and z_i (b,d). MODIS data are shown using solid (NE Pacific) and open (SE Pacific) circles, which represent median values for binned z_i ranges, with dashed and dotted lines respectively indicating 25th and 75th percentiles. Also shown are results from FIRE, EPIC and ASTEX (see text). The gray dashed lines in (b) and (d) are parameterizations described in the text.

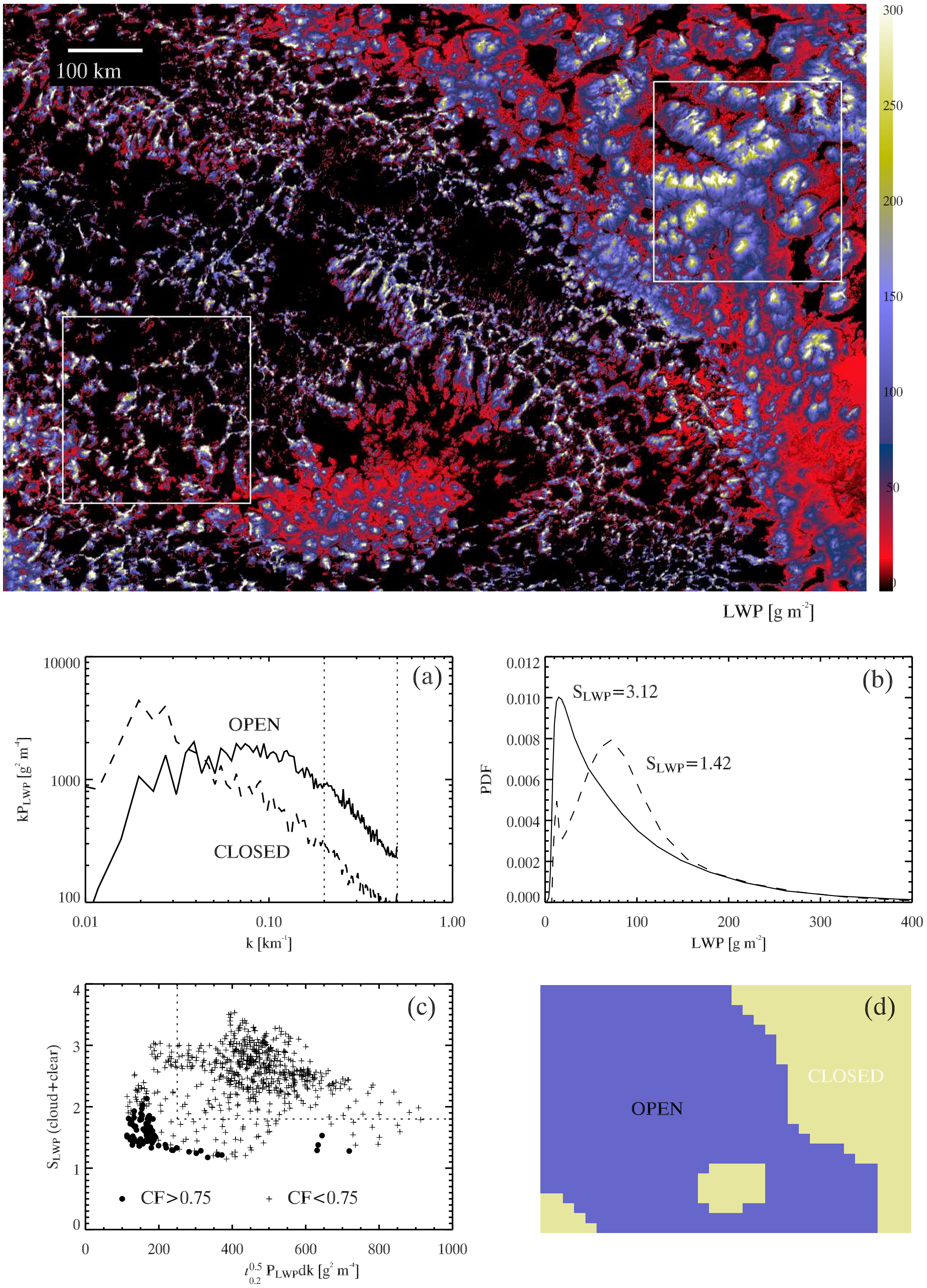

100 km
LWP [g m-2]
(a)
OPEN
CLOSED
kP_LWP [g2 m-4]
k [km-1]
(b)
S_LWP=3.12
S_LWP=1.42
PDF
LWP [g m-2]
(c)
S_LWP (cloud+clear)
CF>0.75
CF<0.75
(d)
OPEN
CLOSED

Figure 1:

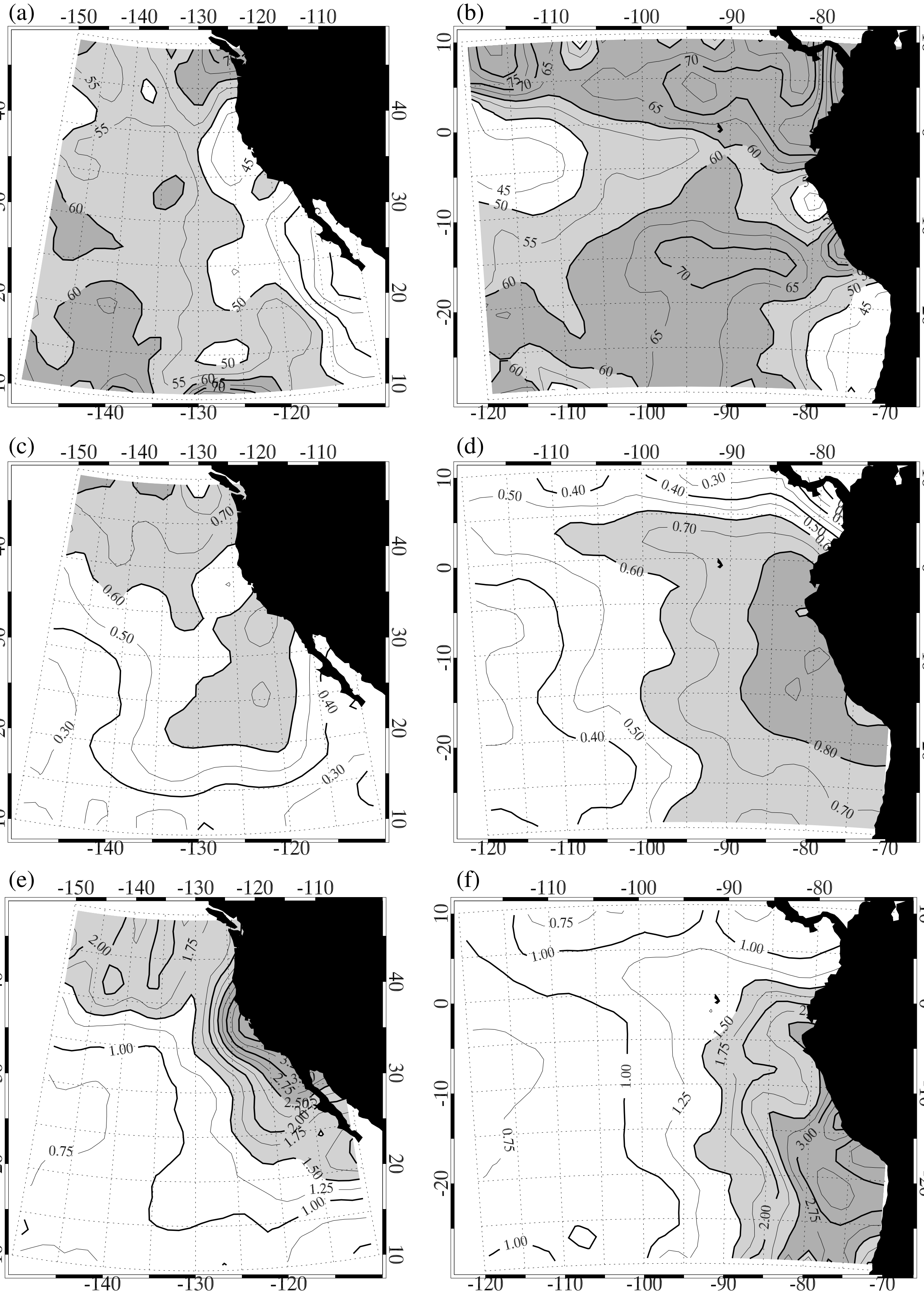
(a)
-150 -140 -130 -120 -110
-140 -130 -120
10 20 30 40
(b)
-110 -100 -90 -80
-120 -110 -100 -90 -80 -70
10 0 -10 -20
(c)
-150 -140 -130 -120 -110
-140 -130 -120
10 20 30 40
(d)
-110 -100 -90 -80
-120 -110 -100 -90 -80 -70
10 0 -10 -20
(e)
-150 -140 -130 -120 -110
-140 -130 -120
10 20 30 40
(f)
-110 -100 -90 -80
-120 -110 -100 -90 -80 -70
10 0 -10 -20

Figure 2:

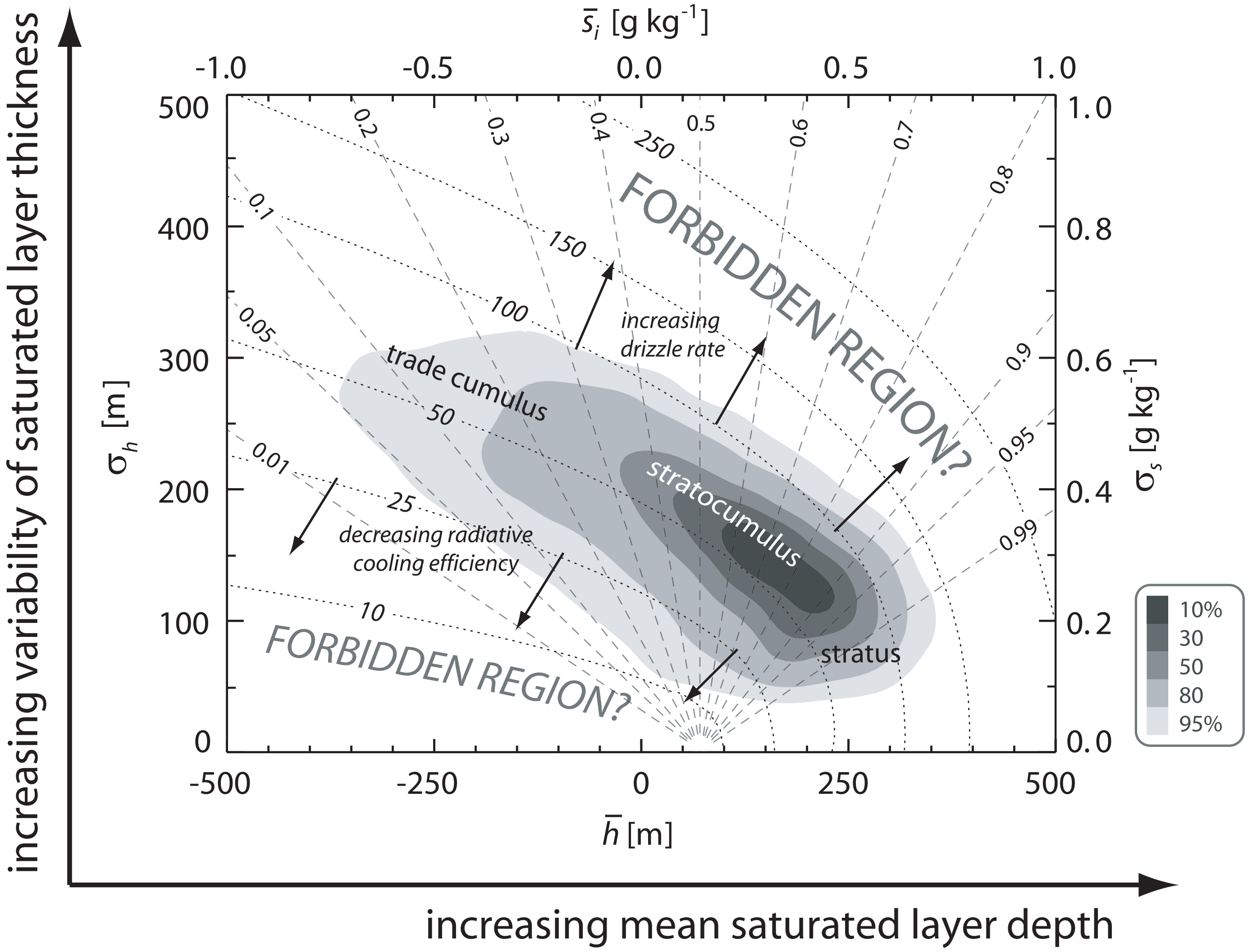
increasing variability of saturated layer thickness
increasing mean saturated layer depth
$\bar{s}_i$ [g kg^{-1}]
σ_h [m]
σ_s [g kg^{-1}]
$\bar{h}$ [m]
FORBIDDEN REGION?
FORBIDDEN REGION?
increasing drizzle rate
decreasing radiative cooling efficiency
trade cumulus
stratocumulus
stratus
10%
30
50
80
95%

Figure 3:

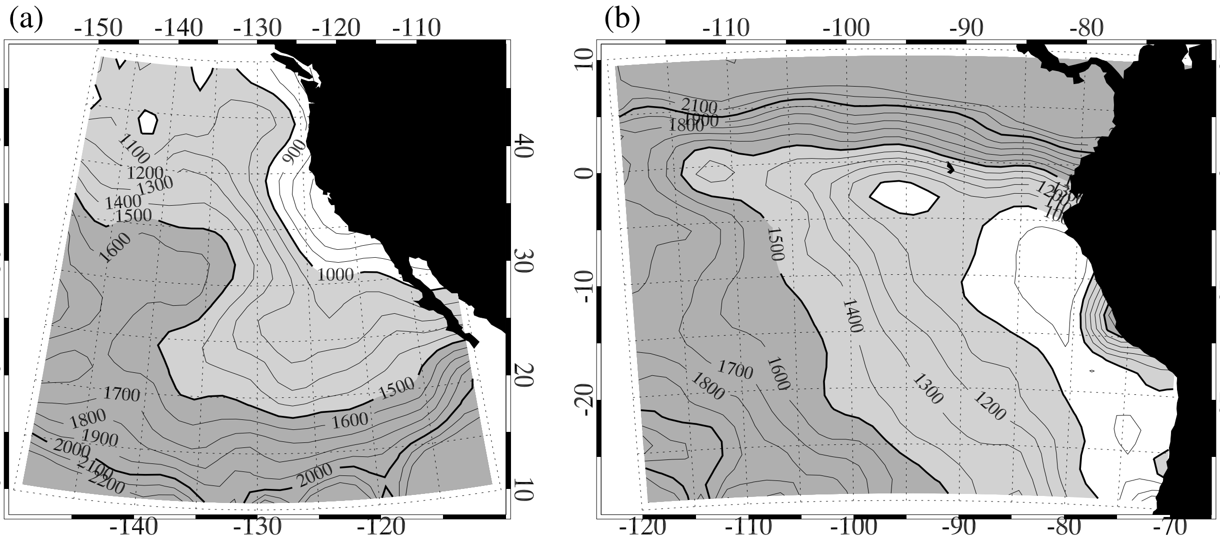

Figure 4:

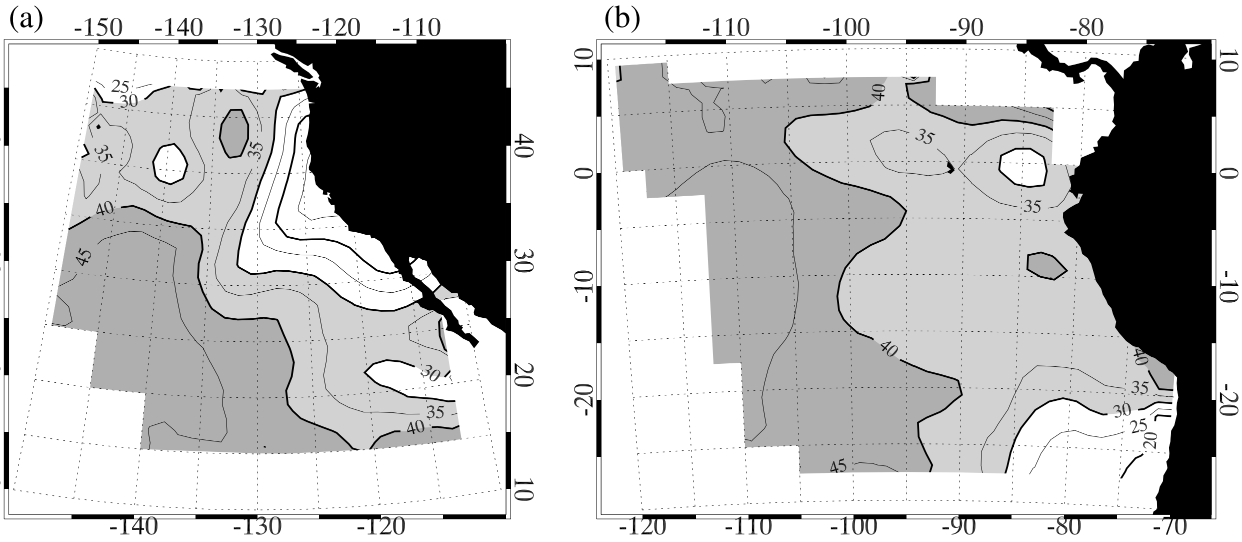
(a)
-150
-140
-130
-120
-110
40
30
20
10
-140
-130
-120
25
30
35
40
45
(b)
-110
-100
-90
-80
10
0
-10
-20
-120
-70
35
40
45
30
25
20

Figure 5:

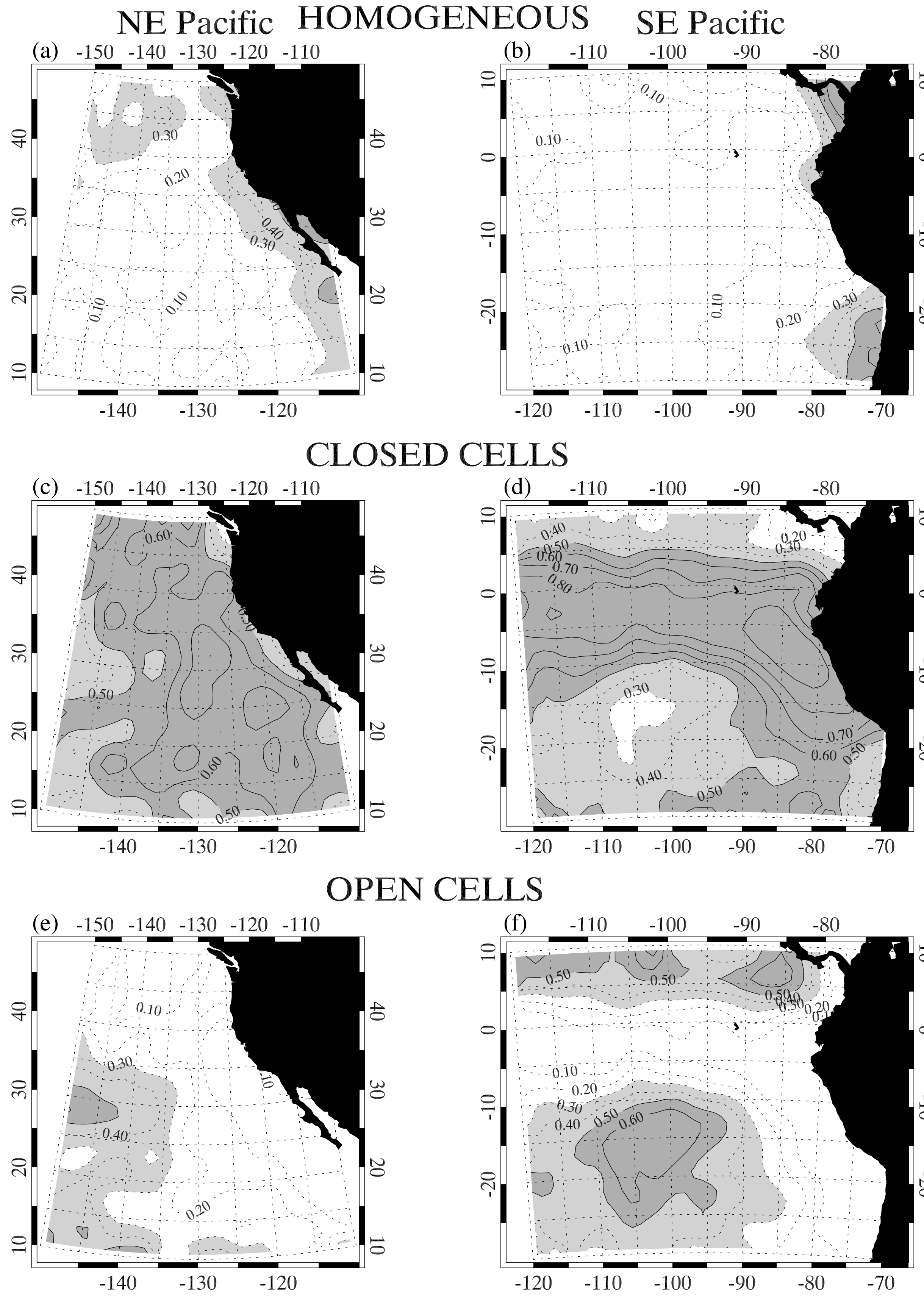
HOMOGENEOUS
NE Pacific
SE Pacific
(a)
(b)
CLOSED CELLS
(c)
(d)
OPEN CELLS
(e)
(f)

Figure 6:

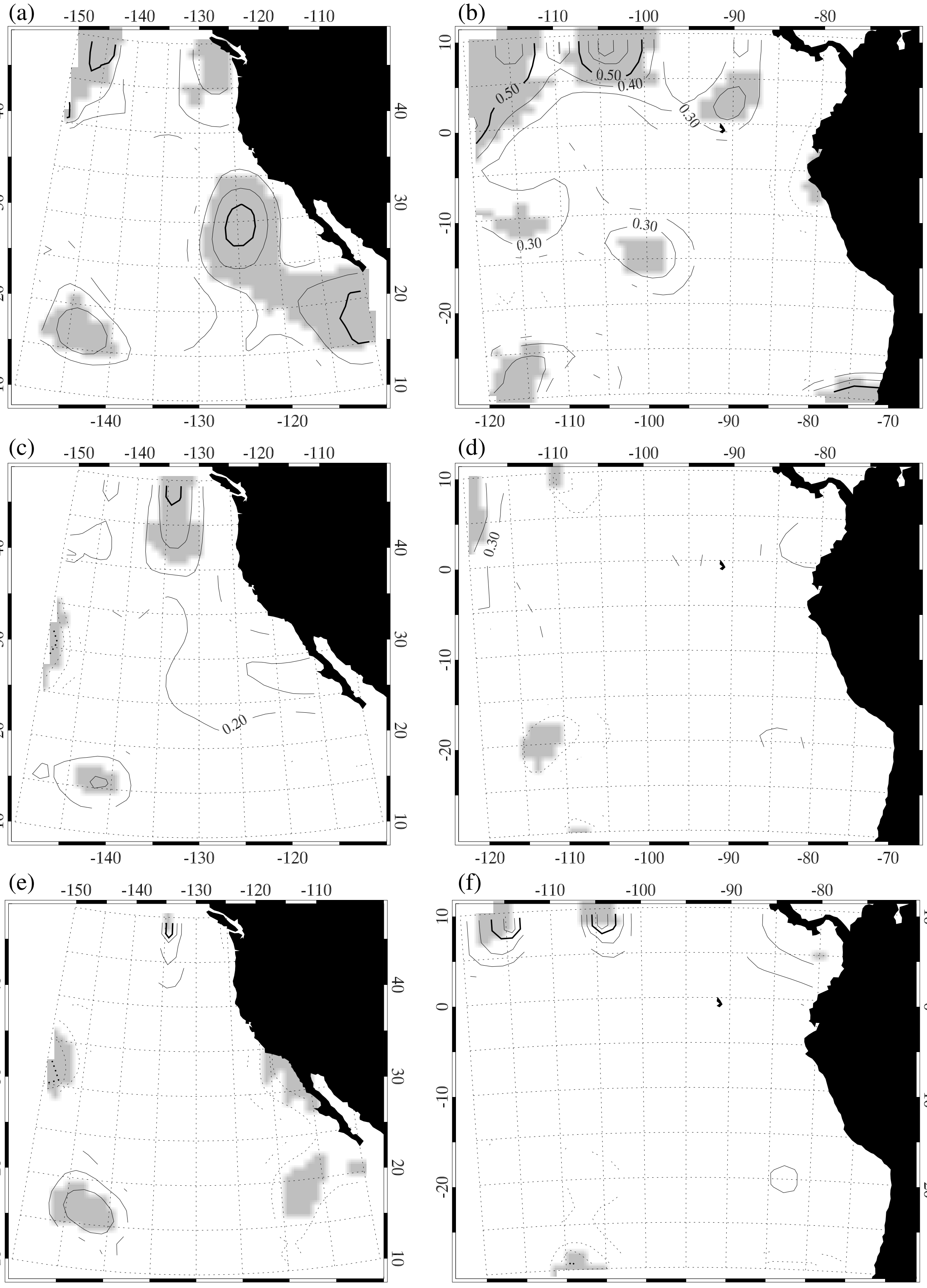
(a)
-150 -140 -130 -120 -110
-140 -130 -120
10 20 30 40
(b)
-110 -100 -90 -80
-120 -110 -100 -90 -80 -70
10 0 -10 -20
0.50
0.50
0.40
0.30
0.30
0.30
(c)
-150 -140 -130 -120 -110
-140 -130 -120
10 20 30 40
0.20
(d)
-110 -100 -90 -80
-120 -110 -100 -90 -80 -70
10 0 -10 -20
0.30
(e)
-150 -140 -130 -120 -110
-140 -130 -120
10 20 30 40
(f)
-110 -100 -90 -80
-120 -110 -100 -90 -80 -70
10 0 -10 -20

Figure 7:

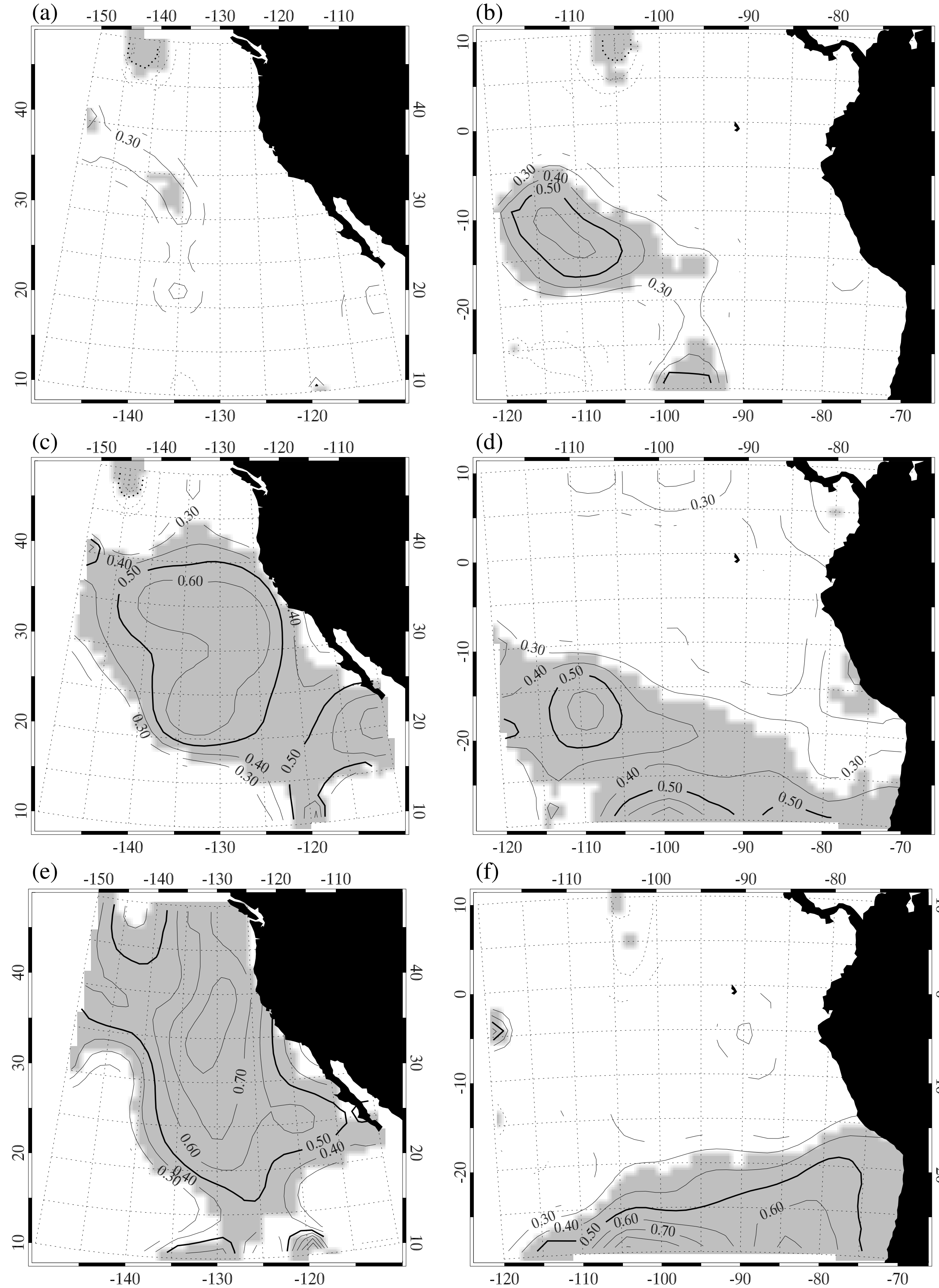

Figure 8:

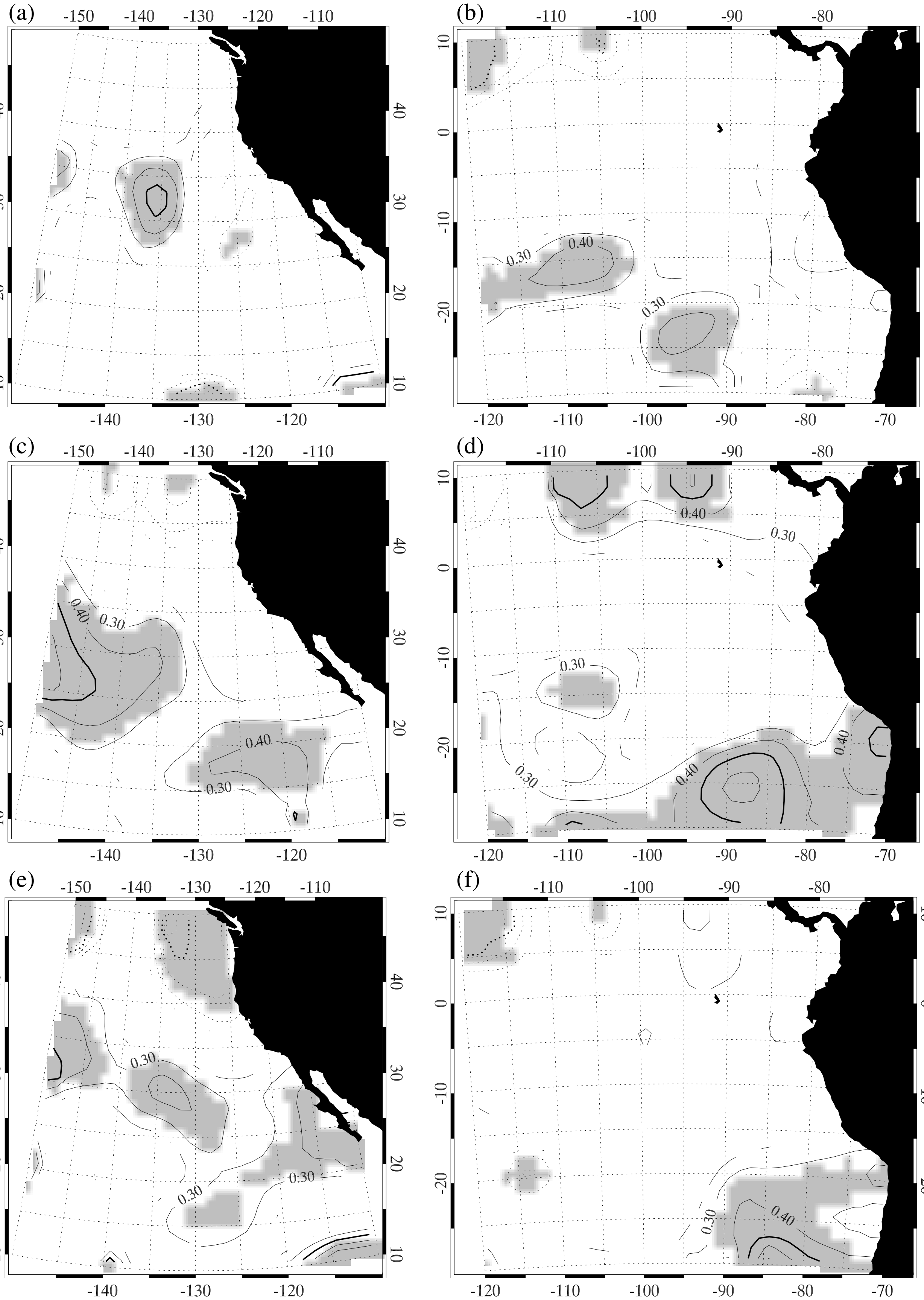
(a)
(b)
0.30
0.40
0.30
(c)
0.40
0.30
0.40
0.30
(d)
0.40
0.30
0.30
0.30
0.40
0.40
(e)
0.30
0.30
0.30
(f)
0.30
0.40

Figure 9:

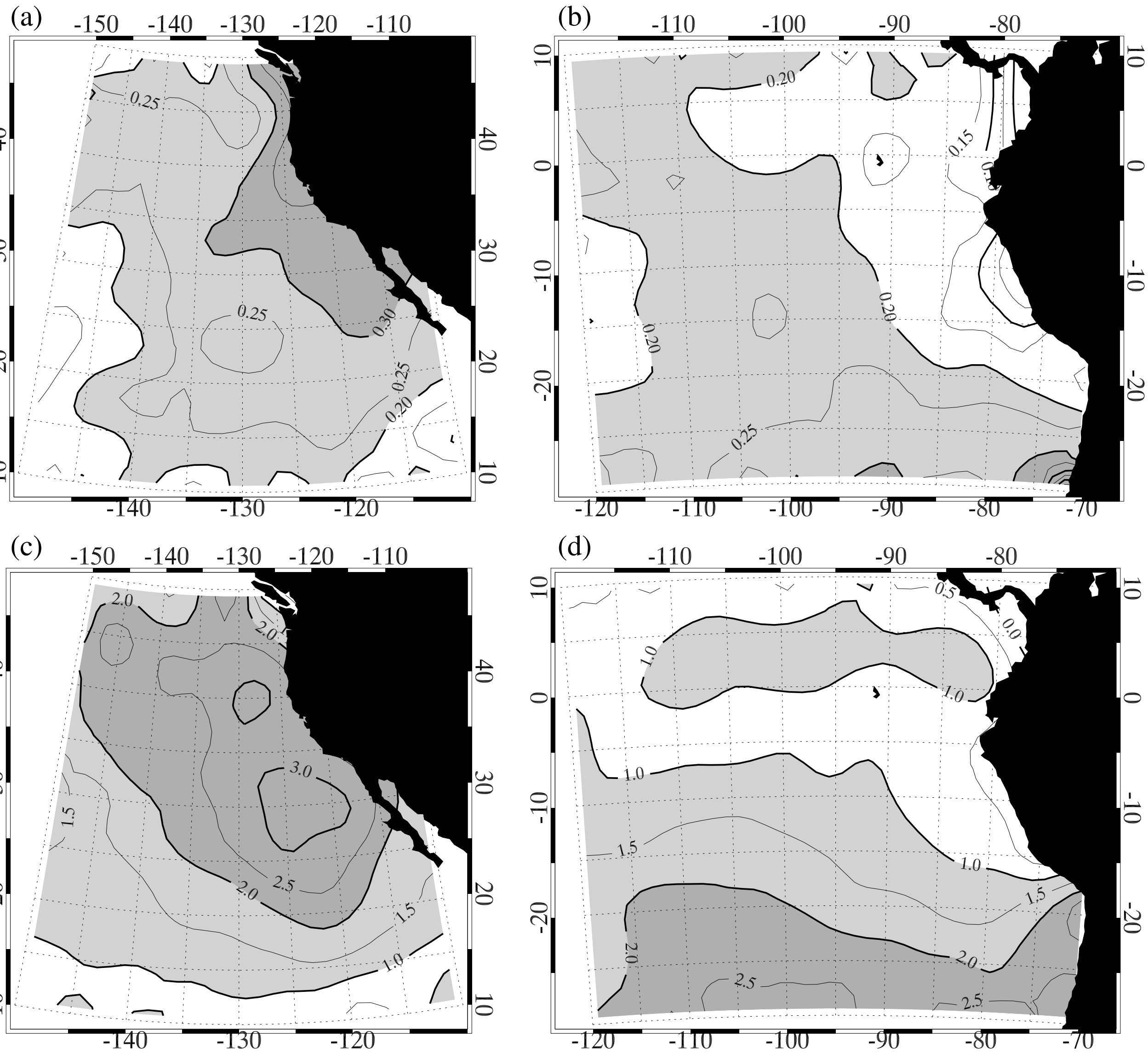

Figure 10:

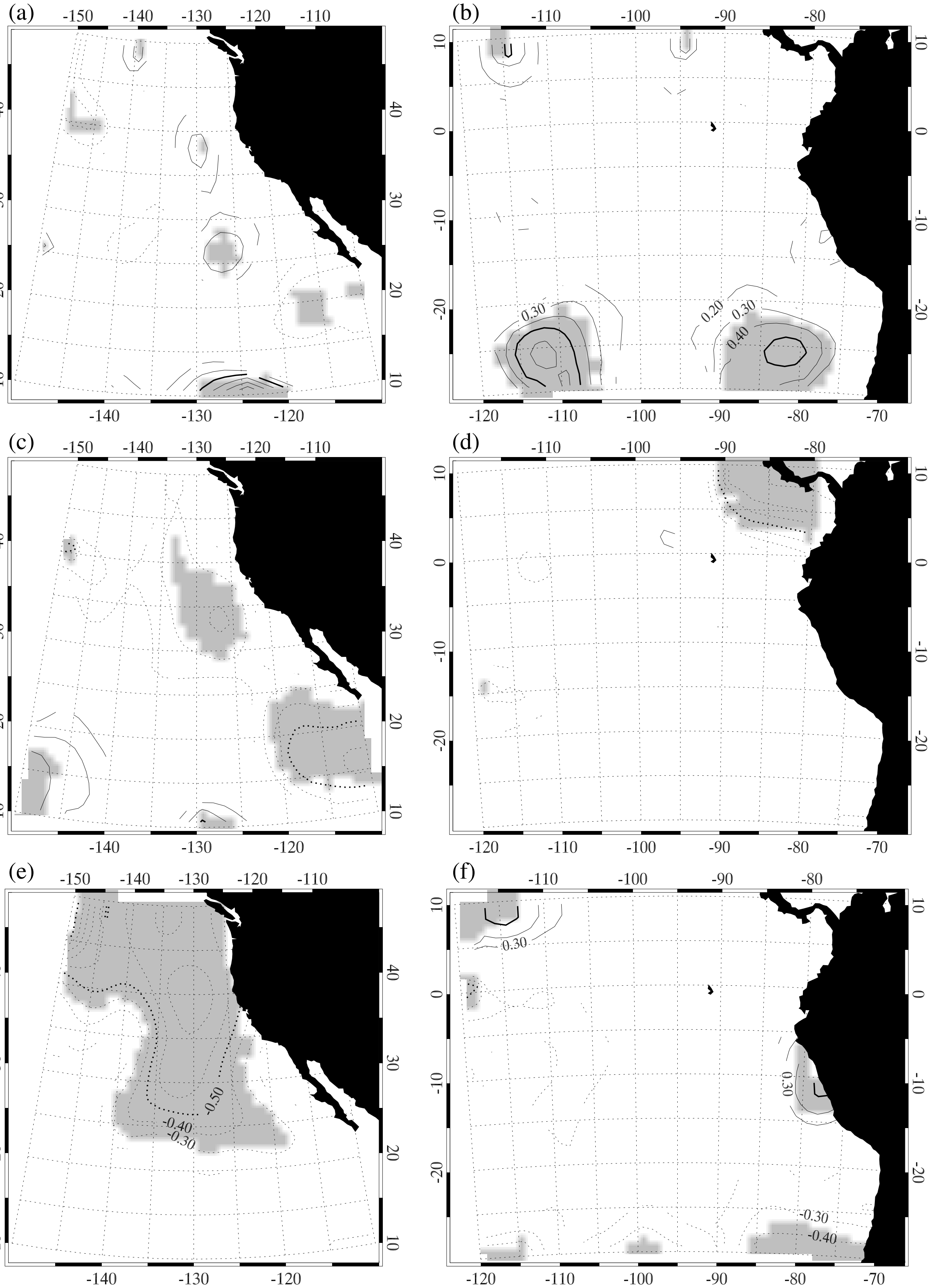

Figure 11:

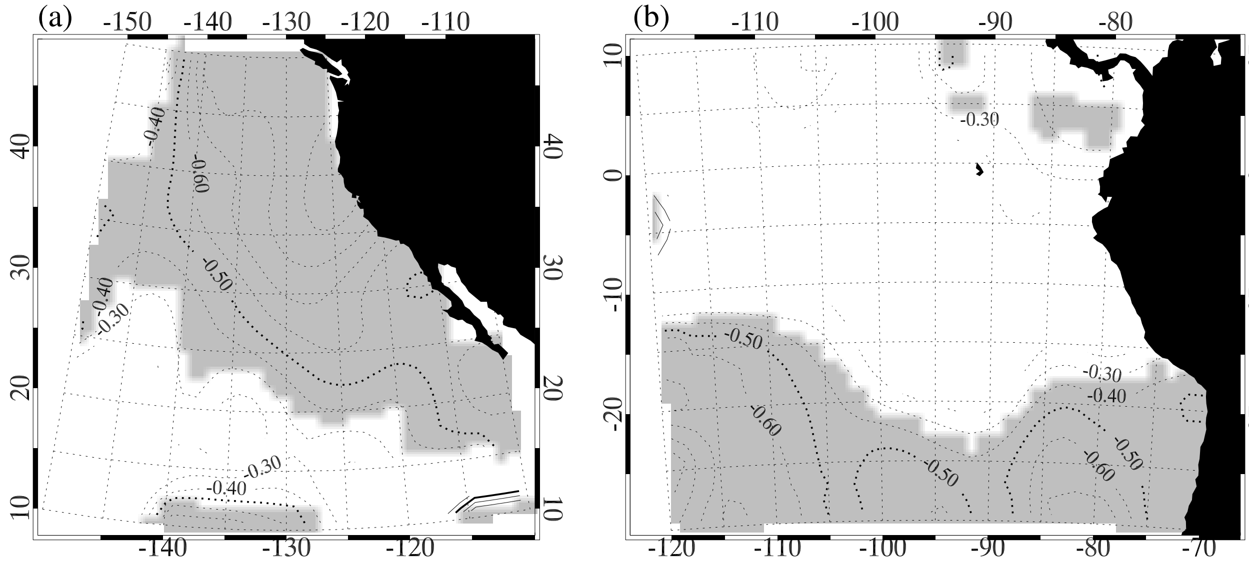
(a)
-150
-140
-130
-120
-110
-140
-130
-120
10
20
30
40
-0.40
-0.60
-0.50
-0.40
-0.30
-0.30
-0.40
(b)
-110
-100
-90
-80
-120
-110
-100
-90
-80
-70
10
0
-10
-20
-0.30
-0.50
-0.60
-0.50
-0.30
-0.40
-0.50
-0.60

Figure 12:

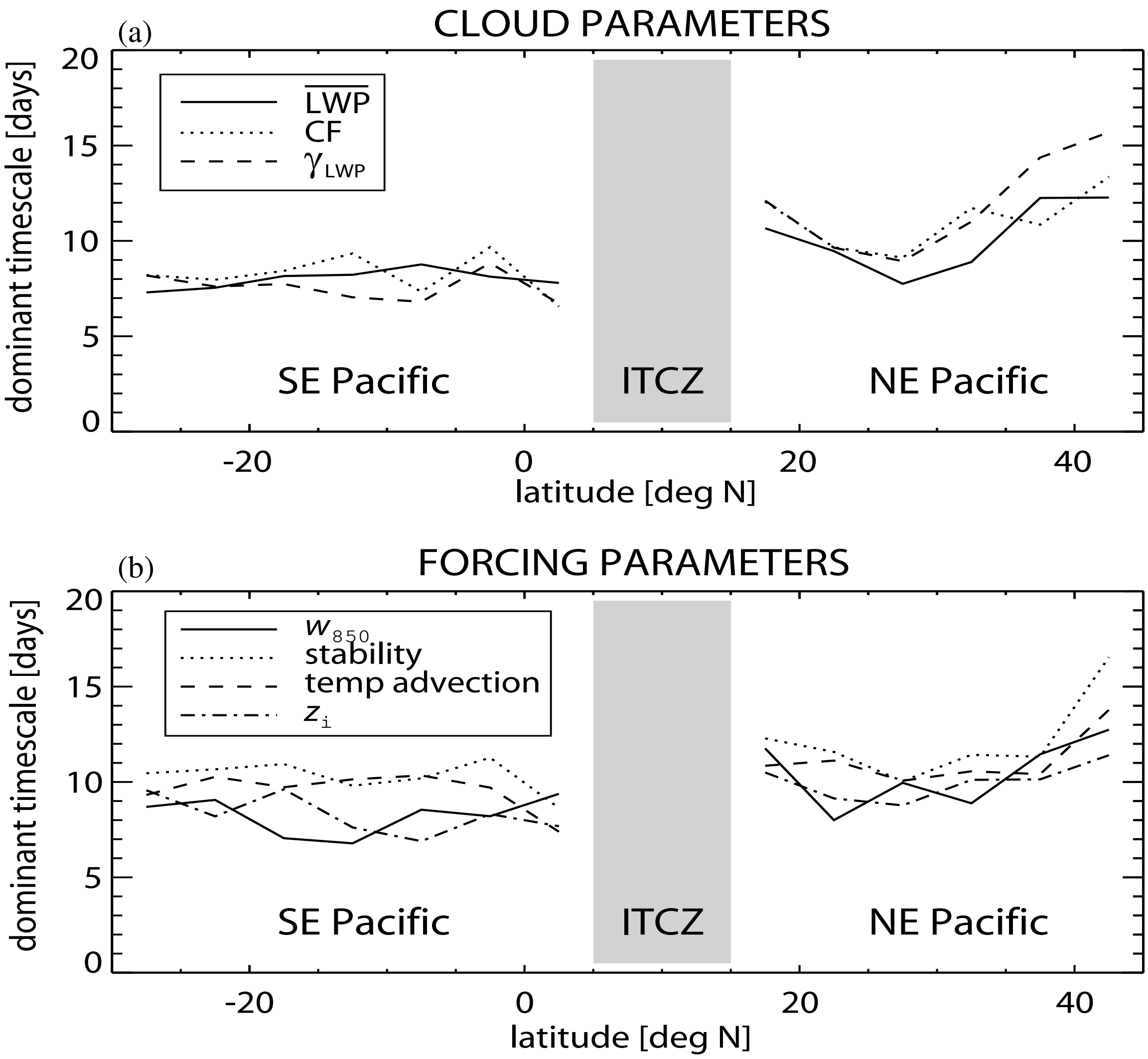

(a)
CLOUD PARAMETERS
dominant timescale [days]
LWP
CF
γLWP
SE Pacific
ITCZ
NE Pacific
latitude [deg N]
(b)
FORCING PARAMETERS
dominant timescale [days]
w850
stability
temp advection
zi
SE Pacific
ITCZ
NE Pacific
latitude [deg N]

Figure 13:

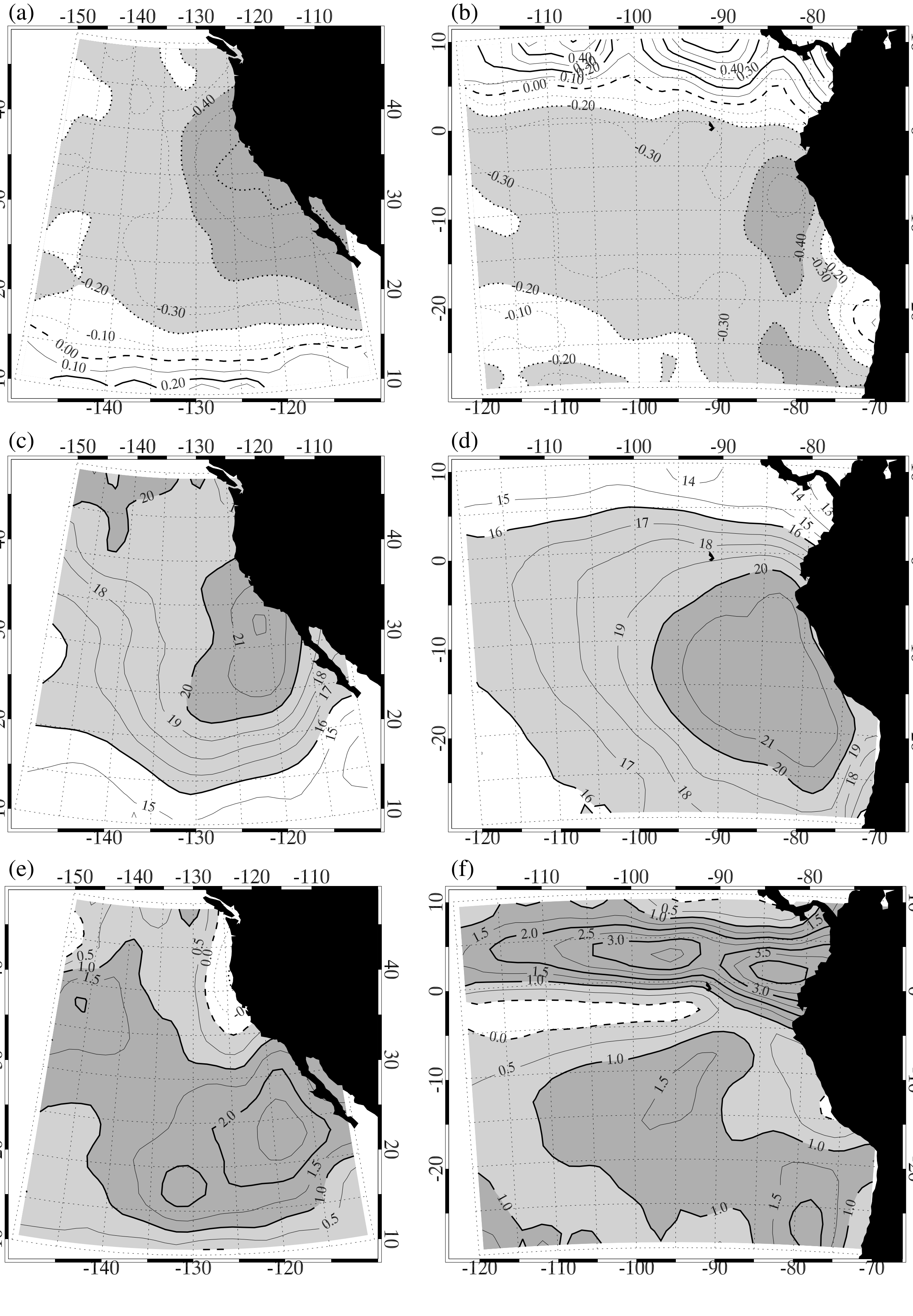

Figure 14:

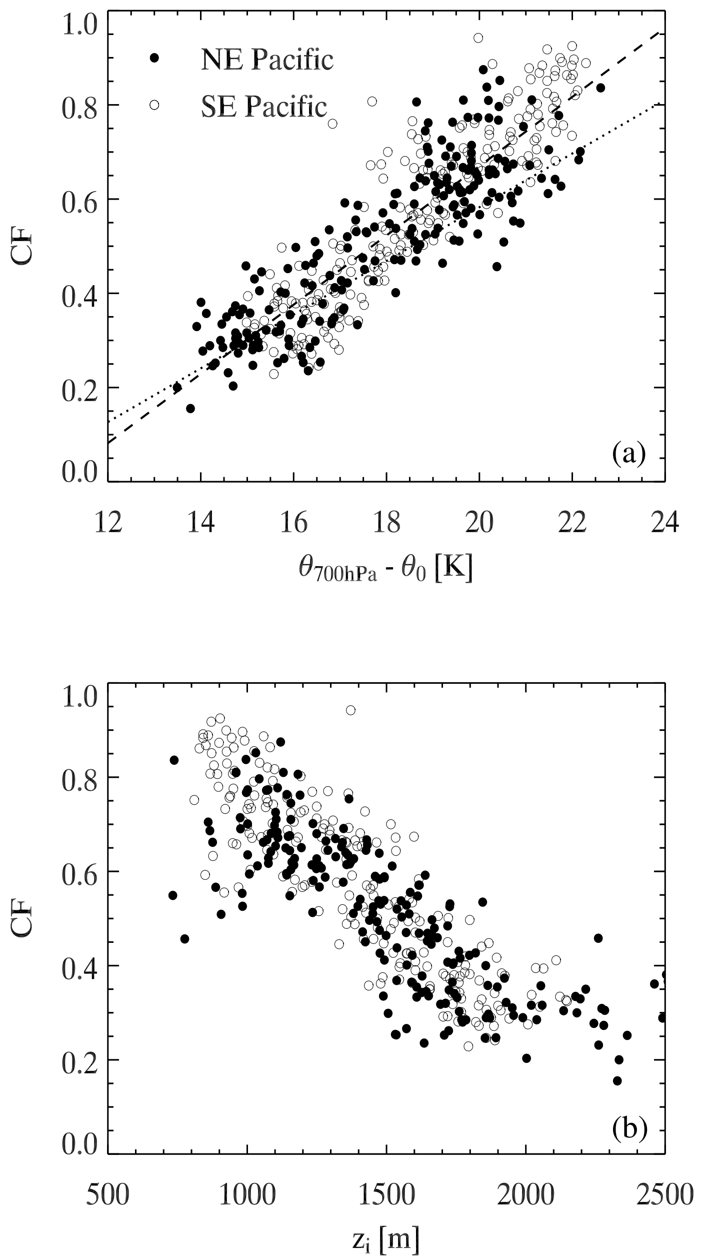

Figure 15:

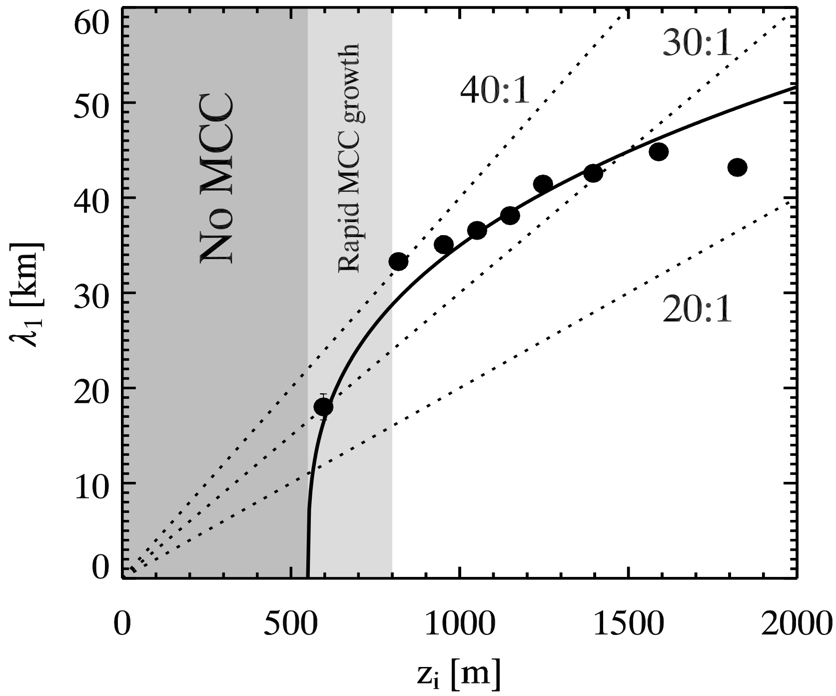

60
50
40
30
20
10
0
0
500
1000
1500
2000
λ_1 [km]
z_i [m]
No MCC
Rapid MCC growth
40:1
30:1
20:1

Figure 16:

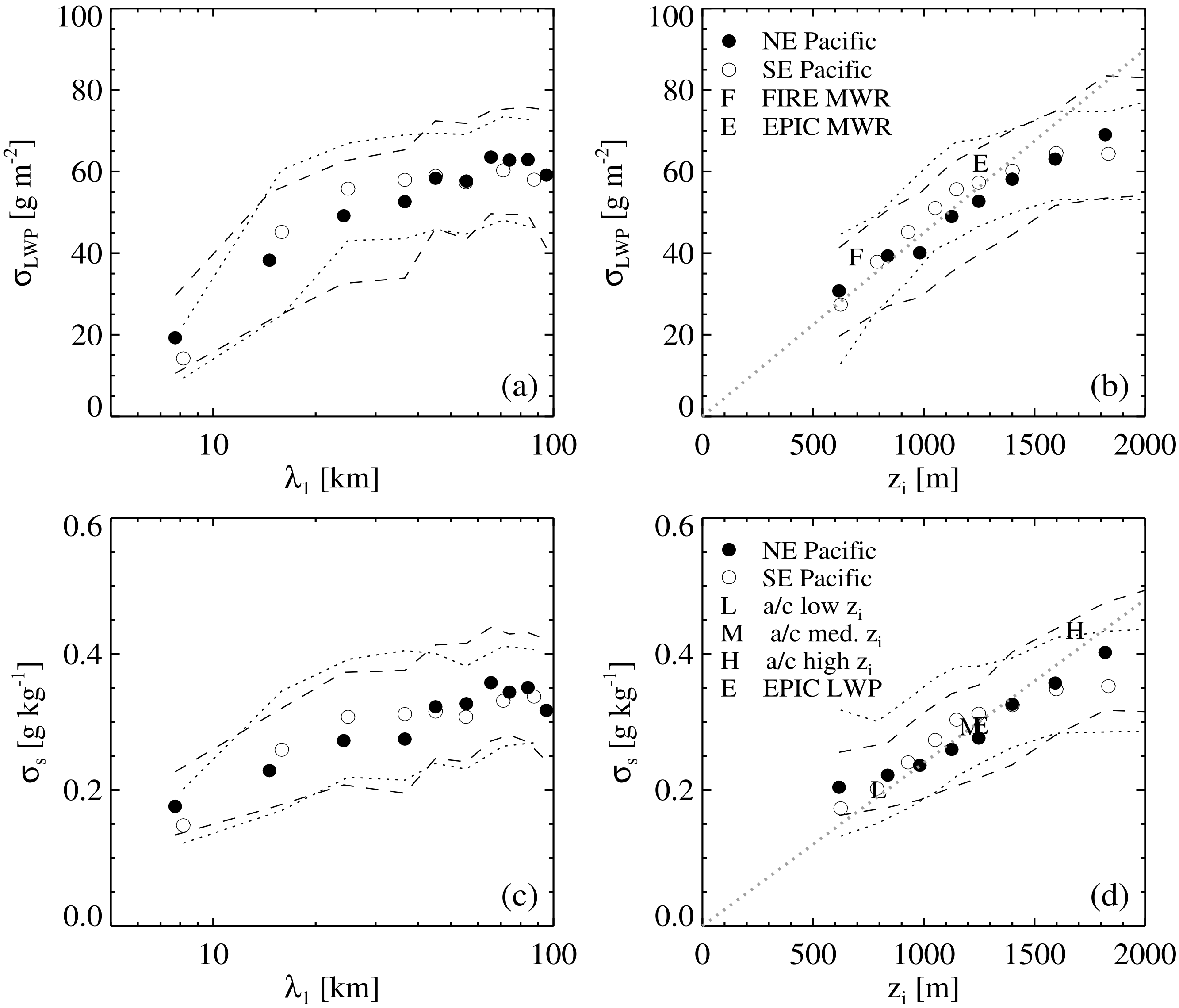

NE Pacific
SE Pacific
F FIRE MWR
E EPIC MWR
L a/c low z_i
M a/c med. z_i
H a/c high z_i
E EPIC LWP
(a)
(b)
(c)
(d)
σ_{LWP} [g m^{-2}]
σ_s [g kg^{-1}]
λ_1 [km]
z_i [m]

Figure 17: